coatings

MDPI

Article

Mixed Films Based on MgO for Secondary Electron Emission Application: General Trends and MOCVD Prospects

Inga G. Vasilyeva [1,*], Evgeniia S. Vikulova [1], Alena A. Pochtar [2] and Natalya B. Morozova [1]

[1] Nikolaev Institute of Inorganic Chemistry, Russian Academy of Sciences, Siberian Branch, Ac. Lavrentiev Ave. 3, 630090 Novosibirsk, Russia; lazorevka@mail.ru (E.S.V.); mor@niic.nsc.ru (N.B.M.)
[2] Boreskov Institute of Catalysis, Russian Academy of Sciences, Siberian Branch, Ac. Lavrentiev Ave. 5, 630090 Novosibirsk, Russia; po4tar@catalysis.ru
* Correspondence: kamarz@niic.nsc.ru; Tel.: +7-383-330-9712

Abstract: Doping process is widely used to improving emission performance of MgO films thicker than 10 nm via assisting the surface recharge and changing in electron structure. The present paper briefly reviews this strategy in a search for the new materials and structures being effective for secondary electron emission (SEE) and their diagnostics. Then, Metal-Organic Chemical Vapor Deposition (MOCVD) coupled with the specially selected precursor is suggested here as a new technique that transforms the refractory oxides to nanoscale, defect-disordered materials able to solid-solid interaction at 450 °C. Primary experiments have been performed for demanded mixed films based on MgO with ZrO_2 and CeO_2 additions. A dopant impact on facilitating the formation of oxygen vacancies in the host oxide and on the features of new mixed phases have been studied by new diagnostic means, based primarily on chemical method of differential dissolution. The method brought out the effective solvents that were the probes for identifying the nanoscale and amorphous phases possessing by the different defects on the surface of MgO films and determining contents of these phases. This approach allowed us to explain the origin of mixed phases and to estimate contribution of each from them in the macroscopic SEE properties.

Keywords: secondary electron emission; magnesium oxide; doped films; composite films; chemical vapor deposition; chemical method of phase analysis; cerium dioxide; zirconium dioxide

check for updates

Citation: Vasilyeva, I.G.; Vikulova, E.S.; Pochtar, A.A.; Morozova, N.B. Mixed Films Based on MgO for Secondary Electron Emission Application: General Trends and MOCVD Prospects. *Coatings* **2021**, *11*, 176. https://doi.org/10.3390/coatings11020176

Academic Editor: Alessandro Patelli
Received: 14 December 2020
Accepted: 28 January 2021
Published: 2 February 2021

Publisher's Note: MDPI stays neutral with regard to jurisdictional claims in published maps and institutional affiliations.

Copyright: © 2021 by the authors. Licensee MDPI, Basel, Switzerland. This article is an open access article distributed under the terms and conditions of the Creative Commons Attribution (CC BY) license (https://creativecommons.org/licenses/by/4.0/).

1. Introduction

Secondary emission is a phenomenon where primary incident particles of sufficient energy, when hitting a surface or passing through some material, induce the emission of secondary particles. This offers significant scientific interest and possesses a number of current and potential optoelectronic applications. Magnesia is one of the main materials studied in this topic since it exhibits high dielectric and second electron emission (SEE) properties and excellent thermal and thermodynamic stability [1,2]. Thin MgO films are very attractive as a protective layer in alternative-current plasma display panels and as effective emission coating on glass microchannel plates (MCPs) [1,3]. The latters are currently ones of the most effective electronic multipliers. These devices are integral parts of an image intensifiers designed to convert an image invisible to the human eye into a visible one and enhance its brightness (thermal imagers, night vision devices, γ-ray converters, etc.). For this application, the ~10 nm films are ideal to achieve high SEE coefficient (SEEC) at relatively low primary electron energy (100–1000 eV) [1]. The studies on the effect of the film thickness on SEEC of MgO and Al_2O_3 deposited by atomic layer method (ALD) clearly indicated the superiority of MgO. Specifically, for 20 nm MgO and Al_2O_3, the maximum SEEC values were 6.9 and 4.1 [1,4]. The III-Y semiconductor compounds including GaAs, GaP, and GaAsP which can be made only with thickness of a few micrometers, would not do for such coatings because their high SEEC may be achieved with extremely high-energy primary electrons being larger than 10 keV [1]. Since the film thickness and SEEC value

are strongly sensitive to deposition conditions forming microstructure and morphology, MgO films synthesized by different methods possess different emission properties. So, SEEC = 8.3 at 1.3 keV was found for MgO nanowires [5]; SEEC of ca. 7 was observed for MgO prepared by pulse metal-organic chemical vapor deposition (MOCVD) [6]; SEEC between 4.8 and 6.9 at 550 eV was found for thin films deposited by ALD [1,7,8]. It should be noted that MgO films prepared by high-energetic and high-temperature techniques show the relatively low SEEC in the range of 3–4 eV, what is unfit for use them as stable emissive coating [9–11].

At the same time, thicker (>10 nm) MgO films are needed to provide the long-time operating under a continuous bombardment of a high-density primary electron beam. This encounters with the surface charging issue and leads to degradation of SEEC. In this case, doping to films MgO is widely used in the hope that combination of dopant and matrix ingredients can provide novel physical and chemical properties. Addition of conducting metal microcrystals to the thick MgO films is suitable for suppressing the surface charging effect due to altering the surface composition and lowering electron affinity (EA). If a dopant dissolved in MgO facilities the formation of different vacancies, changes of bandgap energy (Eg), surface morphology, and density of films occurred. It follows that deposition method has a great effect on these properties. Among reported methods, electron beam evaporation, high temperature deposition, ion-beam assisted deposition and magnetron sputtering are more often used for MgO thin film deposition. However, such MgO films being with the large amount of different kinds of defects exhibit instability under constant electron/ion bombardment and the operating stability and lifetime of the MgO films became not satisfactory for application them as electron multipliers [1,11].

Chemical methods, such as ALD and MOCVD alongside their capabilities to produce oriented nanostructures with controlled dimension of crystallites, show a great potential for generation defective state of thin MgO films [1,12,13]. Advances of ALD in deposition of MgO materials with SEEC greater than 3 on planar substrates and glass MCPs were described in [1,13]. Our recent fundamental investigations have proved that MOCVD combined with the specific precursor can generate at a temperature of 450 °C the surface single oxygen vacancies named as Fs, having the highest defect donor level in energy band of MgO films and induces some oxygen non-stoichiometry in such refractory oxides like RuO_2 and ZrO_2 [14–16]. From this point, new avenues are opened for interaction of the defective-disordered and well-stirred nanoscale crystallites of two oxides deposited by MOCVD to change the SEE properties of the mixed films. The structure of the paper is follows. We started with a review of recent available works devoted to the mixed films in an effort to enhance SEE properties of MgO. The general trends extracted from these references allowed us to select the mixed systems to be the subject of our experiment, to use the MOCVD procedure for the surface lattice reconstruction and to apply a new combination of diagnostic means providing more reliable and correct information on the chemical and phase state of the nanoscale and even amorphous mixed films. These factors as we shall see subsequently are crucial in the macroscopic SEE properties. The correct physicochemical interpretation of the mixed films is large demand in practice and remains a challenging task.

2. General Trends

There is a sufficient number of works where enhancement of SEEC of the relatively thick (>10 nm) MgO films was observed due to lowering EA due to the surface embedded metal. So, composites such as MgO/Au and Au/MgO modified by Zn and Al, showed high SEE, but despite modifying MgO, the films remained to be unstable during functioning [17–24]. The ALD fabrication of the Al_2O_3/MgO and MgO/Nb/MgO laminated composites with encapsulated MgO and nanoscale Nb layers was of interest for coating due to enhancement of SEEC [25,26]. This effect was explained via an occurrence of highly dispersed, conducting impurity Al particles distributed between the matrix grains [25] and via inducing the Fs center by embedded Nb metal in MgO during laser annealing [26].

The other nanoscale metals as Cr, Ti, V, In, and Ta were also able to create Fs centers increasing SEEC of composite although to a lesser degree [26]. The strategy of preparing a Zn-doped MgO layer on the surface of MgO/Au composite resulted in the higher SEEC that was kept constant all the time under continuous electron bombardment of 200 eV, and this improvement was the most effective due to electrical conductivity induced by Zn doping [23].

The idea that enhancement of the SEEC magnitude electron-or ion induced is linked with dissolution of appropriate oxide dopant in MgO, led to occurrence of many works where interaction between mixed oxides taken in pairs was investigated. The increase of SEEC induced by Auger neutralization of He^+, Ne^+, Ar^+ and Xe^+ ions was predicted first of all theoretically for MgCaO, MgSrO, and MgBaO [27]. The higher defect level for Ti-, Cr-, Fe-, Ni- and Zn-doped MgO lying above the valent band of MgO was also calculated to show its advantage for getting larger SEEC and high chemical activity of the doped films from which Ti and Cr appears to be more perspective components [28,29]. The oxides of different valence were tested in the search of the best effect on SEE properties of pure MgO. This was arranged by addition of alkaline metal oxides [30–33], alkaline-earth-metal oxides [34], transition metal oxides [35–38], rare earth oxides [39–45] and others [46–49]. The surprising thing was that results of all the studies after the additives showed a certain enhancement of SEE properties of MgO relate to the pure MgO although often this effect remained without any explanation.

In terms of isovalent and heterogeneous isomorphism, the dissolved oxides with valence lower than MgO should provide the largest effect in generation of the Fs defects in MgO lattice. The experiment with alkaline metal oxides support well this idea: in the mixed MgO films, the F and F^+ defects detected by cathode-luminescent technique were of main source of reducing initial firing voltage and increasing conductivity of the films [30–33]. For two-valent oxides, low solubility as $\leq$1 at.% (more often it is the detection limit rather than the real magnitude) and isovalence solid substituting could not radically alter the oxygen vacancy amount and only lowering EA via surface structural modification was taken to explain the SEEC change [34,36]. Additions of the Sc, Y, La, Nd-ternary-valence rare earth oxides to MgO at 450 °C resulted in amorphous films which had some enhancement of SEEC; it was interpreted due to altering the composition surface [39,44] or as irregular intergranular distribution of nanoscale rare earth (RE) oxide particles on the surface MgO films [36,40]. The last explanation was in the line with results of the high-temperature phase diagrams of the RE_2O_3–MgO systems from which no chemical reactions between these oxides would be expected at solidus temperatures below 1200 °C [41,50]. At the same time, the 99% transmittance in the visible range was found for MgO film doped by the 4.1 at.% of Al^{+3} which was related to the real solid solubility of Al_2O_3 in MgO [46]. The reason for the different behavior of RE^{3+}- and Al-oxides may be linked with different positions of the cations in the electronegativity series and different ionic radii of Al and RE metals: $r(Al^{3+})$ is well smaller than $r(Mg^{2+})$ whereas radii of RE^{3+} are well larger.

The experiments with the four-valent oxide additions such as TiO_2, CeO_2 and ZrO_2 to MgO demonstrated also enhancement of the SEEC films. In terms of crystal chemistry, the solid solubility of these oxides in the MgO lattice should produce the Mg^{2+} vacancies that are acceptors rather than donors [40]. It is reasonable to think that the observed enhancement of SEEC in the mixed oxides which is usually linked with the basicity of MgO surface enriched by active donor centers, resulted from more complex defect structure where total concentration of surface donor sites exceed that of surface acidic sites. However, based on the high-temperature phase diagram for MgO–ZrO_2 system, the solid solubility of ZrO_2 in MgO at 450 °C is highly improbable [51]. For the MgO–CeO_2 system prepared by different ways in the temperature range between 450 and 750 °C, the physical mixture of the individual oxides is more typical situation [42,43,45], although the solid solubility, if any, as less than 4 mass.% and the cubic ceria-based solid solution $(CeMg)O_2$ were detected in the calcined in air sol-gel powders [40,42]. At 1750 °C, for CeO_2 specimen milled and fired together with MgO, the solid solubility was found to be less than 5 mass.% according

to the X-ray diffraction (XRD) study [41]. Most likely that the understanding of the real defect states of these mixed oxide films are far short of optimum and it is the major reason of conflicted description of the acidic-basic behavior of the mixed systems.

More emphasis was given to the ZrO_2–MgO system because ZrO_2 with a lower work function than MgO was able to enhance SEEC and discharge characteristics of the mixed films [28,36,39,47–51]. In Ref. [36], such enhancement was related to the changes in energy band structure and surface properties based only on measuring of electrical and discharge properties of the mixed films relative to the pure MgO with no tangible evidence. In other references, changes in the surface morphology, microstructure, diffraction peaks, the surface and mean compositions were examined together with the discharge and SEE properties. As a result, more information on the mixed films were get although the relationship between physicochemical and physical characteristics did not always showed regular rules and mechanism of improvement remained to be not clarified. In these cases, authors pointed to the necessity of further in depth study to understand which properties of really affect the MgO-base emission characteristics of the films [39,47].

In the light of getting new experimental information on the behavior of the mixed systems, we focused on MOCVD procedure. This approach becomes especially attractive because of the ability of MOCVD to generate the very active Fs defects in MgO in reasonable amount that could minimize negative effect of the acceptors induced by the solid solubility of the oxide dopant in the surface layers of the Mg–*X*–O (*X* = Ce, Zr) films. MOCVD process with magnesium and cerium acetylacetonates as precursors has been used earlier to produce mixed films at 505 °C but it was done in atmospheric air, where the possibility to generate the Fs defects in the surface of MgO film is eliminated totally [43]. In our study, we hope to produce both oxides in the defected-disordered state to accelerate the diffusion process and realize the solid-phase interaction between them. In the expectation of very low amounts of the dissolved oxide dopant, our attention was focused on new diagnostic means able to reliable determining the phase and chemical state of the films.

Analysis of the existing literature showed serious problems in correct characterization of the phase and chemical states of the mixed films possessing a variety of defects that all contribute in enhancement of SEEC. One can see that the Eg of the doped MgO films are linked to either independent but competitive or simultaneously contributing phenomena which are produced from the presences of: (i) oxygen and Mg vacancies; (ii) the varied extend non-stoichiometry; (iii) the various atomic associations in the lattice and (iv) the nanoscale size of the crystallites and microstructure [14,52–54]. Therefore, the powder X-ray diffraction was limited in revealing nanocrystalline size, lattice strain and structural modification of surface because all the characteristics contribute in the brooding, attenuating and shifting of the same peak, and the more so, this method is useless for diagnostics of nanoscale and X-ray amorphous films [37,41]. Notable, that the data on mean and surface chemical composition that are provided by X-ray energy dispersive spectroscopic (EDX) and X-ray photoelectron spectroscopic (XPS) methods becomes distorted with hydroxylation and carboxylation of the films. It is associated with the presence of exceeded oxygen from OH^-- and CO_3^{2-}-groups that shifts and broads the full width-half-maximum of the O 1s core level BE might and increase total oxygen content up to 56 at.% [14,36,37,52,53]. Ultraviolet photoelectron spectroscopy, optics and reflection electron energy loss spectroscopy are also sensitive to the hydroxylation effect and cannot detect selectively individual types of the F defects in the presence of the impurity oxygen atoms [42,48,52,54]. In such a situation, preference was given to differential dissolution (DD) method which inherently performs at once the phase and chemical analyses of the simple and complex films as it was shown before in [14–16,55,56]. Combining DD data with those obtained by XRD, scanning electron microscopy (SEM) and measuring SEEC of the films, we were in the certainty to get the exhaustive structural, chemical and phase information and to explain what the phase component and in what manner contributes in enhancement of SEE properties.

3. Materials and Methods

The mixed oxide films of Mg–X–O systems (X = Zr, Ce) were prepared via MOCVD technique using an original hand-made vertical cold-wall reactor described in the previous papers [14,15]. The experimental conditions used here are shown in Table 1. Specifically, the well-proven complex $Mg(tmeda)(thd)_2$ (tmeda = N,N.N′,N′-tetramethylethylenediamine, thd = 2,2,6,6-tetramethylheptane-3,5-dionato) was used as a magnesium oxide precursor [14,15]. To exclude the ligand exchange during co-deposition process, zirconium(IV) and cerium(IV) volatile precursors with the same β-diketonate anion, $Zr(thd)_4$ and $Ce(thd)_4$, were selected in combination. All the volatile precursors used here were prepared through the common synthetic methods described elsewhere [57,58]. The complexes were purified via double vacuum sublimation and characterized by elemental analysis (CARLO-ERBA-11008). For $Mg(tmeda)(thd)_2$ ($C_{28}H_{54}O_4N_2Mg$, CAS 302351-10-6) found (mass.%): C 66.5, H 11.0, N 5.3; calculated: C 66.3, H 10.7, N 5.5. For $Zr(thd)_4$ ($C_{44}H_{76}O_8Zr$, CAS 18865-74-2) found (mass.%): C 64.1, H 9.0; calculated: C 64.1, H 9.3. For $Ce(thd)_4$ ($C_{44}H_{76}O_8Ce$, CAS 18960-54-8) found (mass.%): C 60.6, H 8.8; calculated (%): C 60.5, H 8.8.

Table 1. MOCVD experimental conditions to prepare Mg–X–O mixed films (X = Zr, Ce).

X	Zr	Ce
X precursor	$Zr(thd)_4$	$Ce(thd)_4$
Source 1 temperature, °C	134–165	140
Magnesium precursor	$Mg(tmeda)(thd)_2$	
Source 2 temperature, °C	110	
$n(Mg)_{precursor}$:$n(X)_{precursor}$ *	2:1–10:1	9:1
Deposition temperature, °C	450–500	450
Deposition time, min	60–120	90
v(Ar), sccm	25 (source 1), 25 (source 2)	
$v(O_2)$, sccm	17	
Total pressure, Torr	10	

* precursor molar ratios calculated from the mass loss in the sources.

Within all the experiments, the temperature and amount of the magnesium precursor source were constant, ensuring that the precursor enters the reactor at a rate of 5×10^{-4} mmol/min. The source temperatures of the zirconium precursor were varied within such a range that its transfer rates were (0.5–2.5) $\times 10^{-4}$ mmol/min. In the case of cerium, test experiments were carried out at a precursor transfer rate of 4.5×10^{-4} mmol/min. The Si(100) plates (1×1 cm^2) were used as substrates. The aging procedures of the as-deposited samples comprised prolonged storage in air (25 °C, relative humidity of 70%) or in a vacuum (25 °C, desiccator, 5×10^{-3} Torr).

The X-ray diffraction (XRD) study of the deposited films was performed on Shimadzu XRD-7000 (Cu$K\alpha$ radiation, Ni filter, $2\theta = 5°$–$60°$) using a common software (PowderCell 2.4 and WINFIT 1.2.1). The morphology was examined by scanning electron microscopy (SEM, JEOL-ISM 6700 F, Tokyo, Japan), and the elemental composition was evaluated by EDX (EX-2300BU, JEOL, Tokyo, Japan). The film thicknesses were estimated from the SEM cross-section. The SEEC measurements were carried out within a range of energy of primary electrons (Ep) of 50–1200 eV as described in the previous works [14,15].

Since the active surface oxygen vacancies and less-coordinated morphological sites are best determined through their different solubility in the acidic solvents, differential dissolution (DD) [14–16,56] was carried out in the specially induced dynamic regime with progressively increasing concentration of solvent, i.e., its chemical potential μ, that provided sequentially transfer of the phases into solution (Figure 1a). The solvent went over a film with a constant velocity, dissolving the ~5 Å/cm^2 layer, and each solvent portion was fed by peristaltic pumps with a frequency of 1 s to the analyzer detector, an inductively coupled plasma atomic emission spectrometer (ICP AES, model 262477-364A, Baird, Zoeterwoude, Holland). The ICP AES analyzer detector determines simultaneously of all elements of the test films except for O ions, with the sensitivity at 10^{-3} μg mL^{-1}, error

at 1%–5% [14,55]. In this experiment, the solvent varied in order of increasing its chemical potential from water to 0.01 N HCl, then to 3 N HCl, and finally to 3 N HF with progressive heating from 20 to 80 °C. The HF acid was held to be a good solvent for bulk stoichiometric ZrO_2 and CeO_2 [55]. The metal cations were determined in 200–300 portions, and the kinetic curves were constructed from which the phase state and elemental stoichiometry of solid oxide species were revealed. The defected oxides with more basic character (Figure 1, blue and green peaks) than stoichiometric oxides (Figure 1, red peak) are dissolved either in hot water or in more weak acids like 0.01 N HCl for MgO (Figure 1c) and 3 N HCl for ZrO_2 (Figure 1b). As a result, we consider 3 N HCl as a probe of the defective ZrO_2, whereas 3–4 N HF is a probe of stoichiometric ZrO_2. The hot water is a sensitive probe for MgO modified by the Fs defects, 0.01 N HCl is a probe for oxide whose surface is modified by CO_3^{2-} and 3 N HCl is a probe for Mg-carbonate.

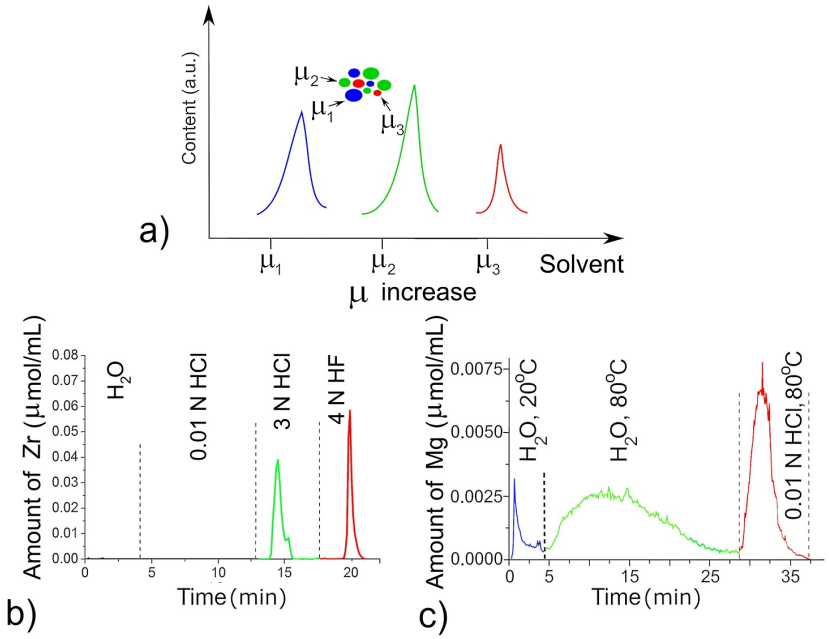


Figure 1. Differential dissolution of the phases with chemical potentials μ_1–μ_3 from a model three-phase mixture (**a**); dissolution of defective (green) and stoichiometric (red) ZrO_2 species (**b**) and dissolution of defective (green) and stoichiometric (red) MgO species (**c**).

4. Results

To understand the key parameters controlling surface state of the mixed films during MOCVD, we could invoked the equilibrium diagrams with the partial pressure of all volatile species for the $Mg(tmeda)(thd)_2$ decomposing in vacuum and oxygen, which were calculated for the molar $n_{O2}/n_{precursor}$ ratio equal to 15 and total pressure 10 Torr (Figure 2a,b). Figure 2b demonstrates the gas-phase medium at 450 °C (723 K) consisting mainly from CO, H_2 species with total pressure of close to 10 Torr and where CO_2 and H_2O have low contents. This gas medium, as almost free from oxygen, generates the Fs defects in MgO, which are the strong basic sites and active donors of electrons [14]. Addition of another precursor such as $Zr(thd)_4$ changes of the gas medium through the formation of quite stable CH_x, $C(CH_x)$ gas species [59–62] that are converted to CO_2 and H_2O molecules during MOCVD process increasing the amounts of undesired carbon dioxide species. These molecules adsorb easily firstly on very active morphological sites, and then, on the Fs defects, when the first sites are already occupied. Thus, for the mixed films, a high probability occurs that with increasing of CO_2 in the gas medium, carboxylation will be extended to the basic Fs sites reducing their donor activity. In this case, the morphological active sites of the mixed films being good tarps of CO_2 vapor acquire importance to keep the Fs defects and ensure a high SEEC.

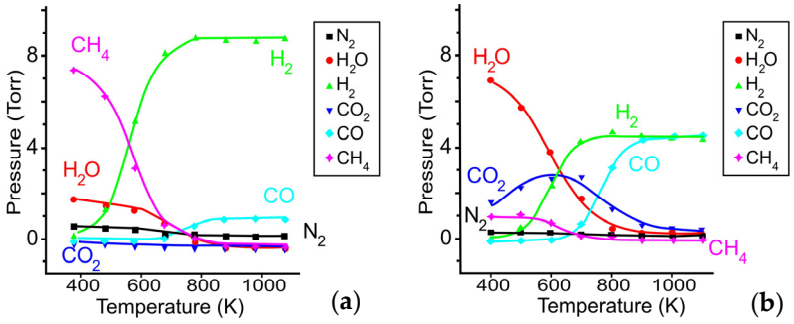


Figure 2. Partial pressures of volatile species versus temperature for the Mg(tmeda)(thd)$_2$ precursor decomposed in vacuum (**a**) and in oxygen (**b**). Adapted with permission from [14]. Copyright 2020 American Chemical Society.

A considerable data capacity on the mixed films prepared at different conditions for the MgO–ZrO_2 and MgO–CeO_2 systems was carried out using XRD, DD, and SEM along with EDX technique and measurements of SEEC. In this paper, only several examples are shown that were the most interesting in the context of studying the mixed films (Figures 3–7).

The XRD patterns of the films (Figures 3c, 5c, 6c and 7c) confirmed the presence of periclase cubic single-oriented MgO due to the only low-intense (200) MgO peak. Otherwise, no film-related reflexes are present (Figure 4c). From this (200) peak, the lattice parameters and the crystallite sizes as coherent scattering ranges were estimated to varied from 4.211(3) Å and 75(8) nm (Figure 5) to 4.192(3) Å and 13(1) nm (Figure 6) for Mg–Zr–O films. The lattice parameter of bulk MgO is 4.213 Å, while for the previously MOCVD-obtained MgO films with the Fs defects it was 4.203(5) Å that was explained by the vacancy occurrence [14]. This shrunk lattice parameter is probably associated with the Zr^{4+} incorporation generating the oxygen vacancies due to shifting oxygen ions towards Zr^{4+} cations with weakening Mg–O binding. The compressive stresses generating vacancies in MgO on Mg^{2+} substitution by any four-valent cations is well-known [42]. However, to support this idea on the substitution effect, the Zr presence in MgO should be determined by other means.

The growth rate of the Mg–Zr–O films varied in the range of 1.5–3.0 nm/min resulting in 90 nm thickness (Figure 4) or in 230–250 nm (Figures 3, 5 and 6). For the Mg–Ce–O film, the growth rate was 1.8 nm/min and thickness ~160 nm. From Figures 3a, 4a, 5a, 6a and 7a one can see that there is some difference among morphologies of the mixed films and their morphologies do not resemble with morphology of the pure MgO film that was represented by the 100 nm uniform quadrangle polyhedral particles [14]. The films are composed of (i) quadrangle irregular in size polyhedral particles being big (250–300 nm) and small (<100 nm) (Figure 3a); (ii) plane-parallel plates uniform in size (Figures 5a and 7a); (iii) sphere large agglomerates composed from fine particles (Figure 6a) and (iv) very fine particles which were x-ray amorphous according to XRD pattern (Figure 4a). The pore structure formed by void spaces between polyhedral particles and agglomerates reduces in the following sequence: Figure 5a → Figure 6a → Figure 4a → Figures 3a and 7a and its changes depend on zirconium content (Table 2). According to the surface SEM images, the surface roughness increases in the following sequence: Figure 6a → Figure 5a → Figure 7a → Figure 4a → Figure 3a, although the cross-sectional SEM images of the films demonstrate a columnar growth and a smooth interface between columns. These characteristics demonstrate that the polyhedral particles possess more morphological defects that are manifested as configuration of edges, corners or crystal planes. SEM examination added little to detect particles like ZrO_2 or CeO_2.

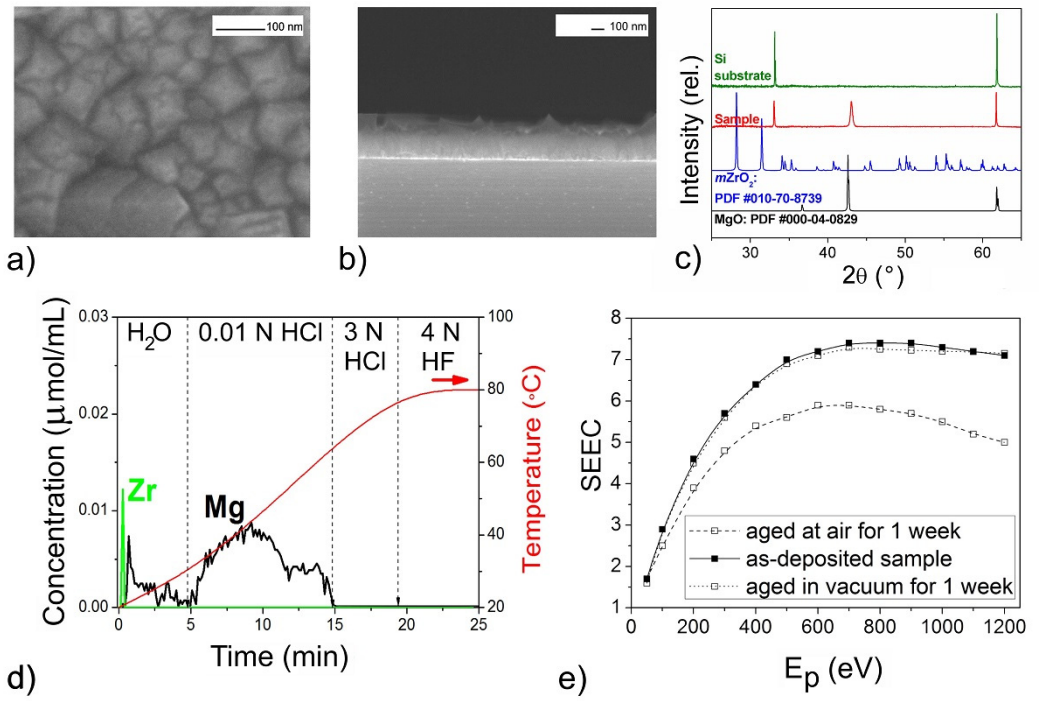


Figure 3. The mixed oxide film with n(Mg):n(Zr) = 50 according to DD data: SEM images (**a**,**b**), XRD pattern (**c**), DD curves (**d**), SEEC-E_p curves (**e**).

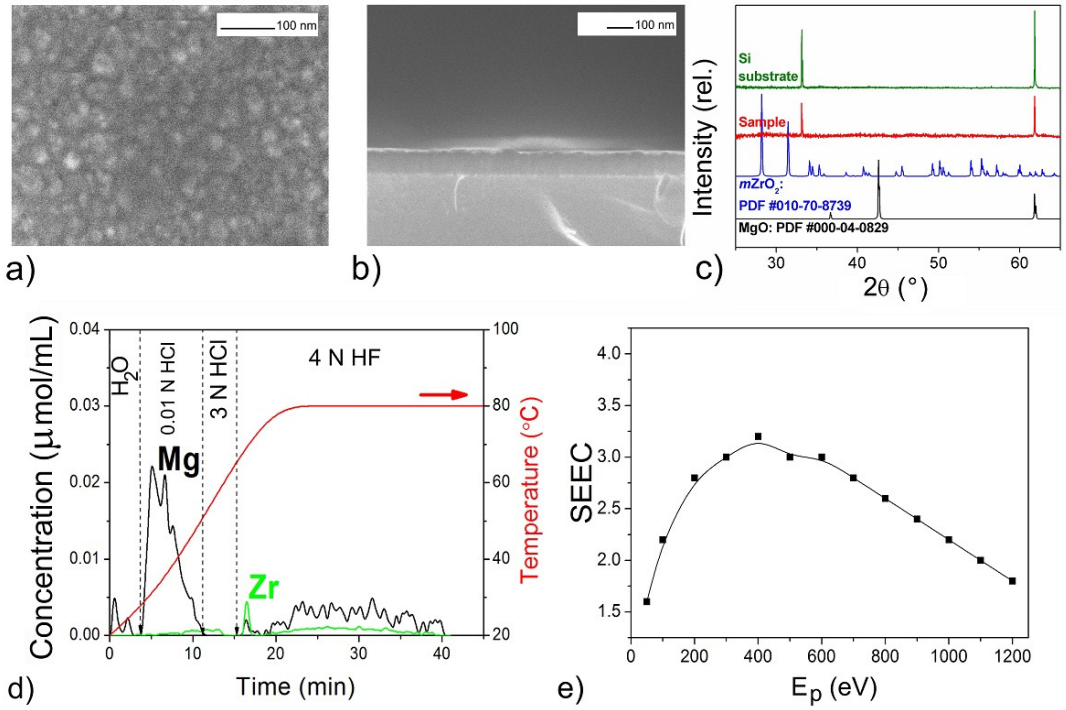


Figure 4. The mixed oxide film with n(Mg):n(Zr) = 11:9 according to DD data: SEM images (**a**,**b**), XRD pattern (**c**), DD curves (**d**), SEEC (Ep) curves (**e**).

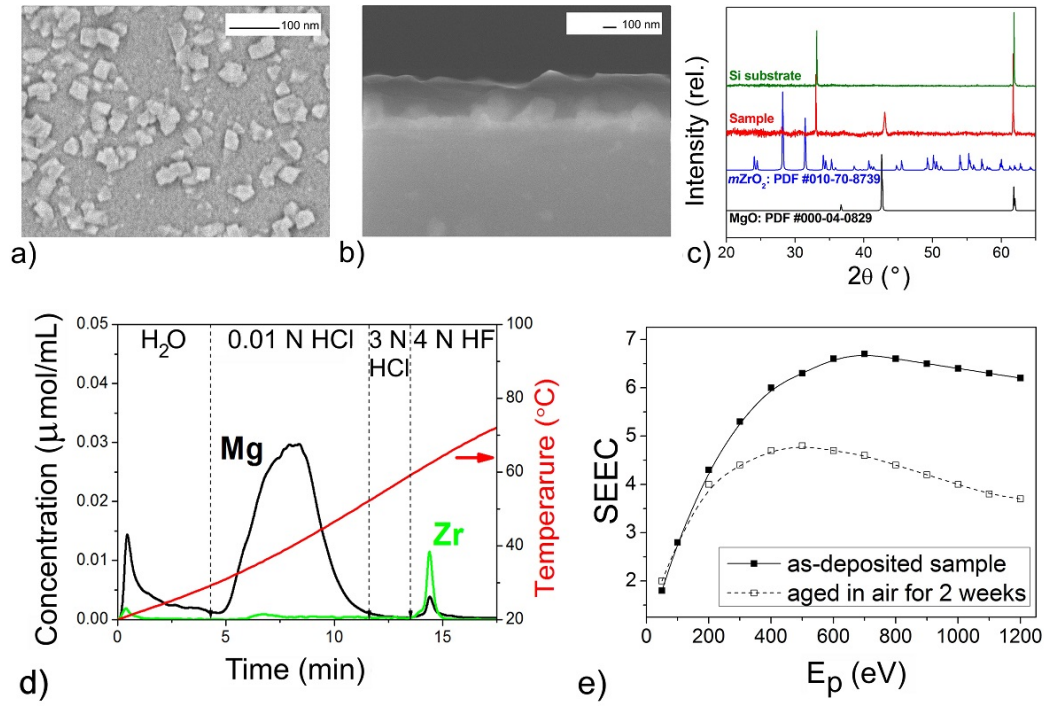


Figure 5. The mixed oxide film with n(Mg):n(Zr) = 11:1 according to DD data: SEM images (**a**,**b**), XRD pattern (**c**), DD curves (**d**), SEEC (Ep) curves (**e**).

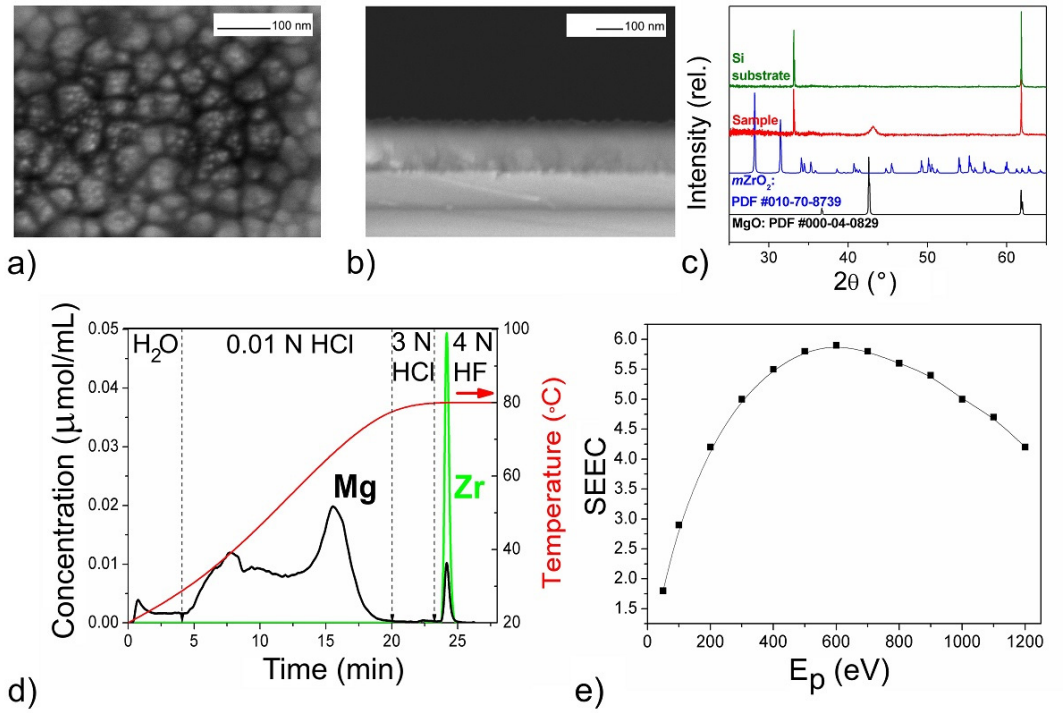


Figure 6. The mixed oxide film with n(Mg):n(Zr) = 10:1 according to DD data: SEM images (**a**,**b**), XRD pattern (**c**) DD curves (**d**), SEEC (Ep) curves (**e**).

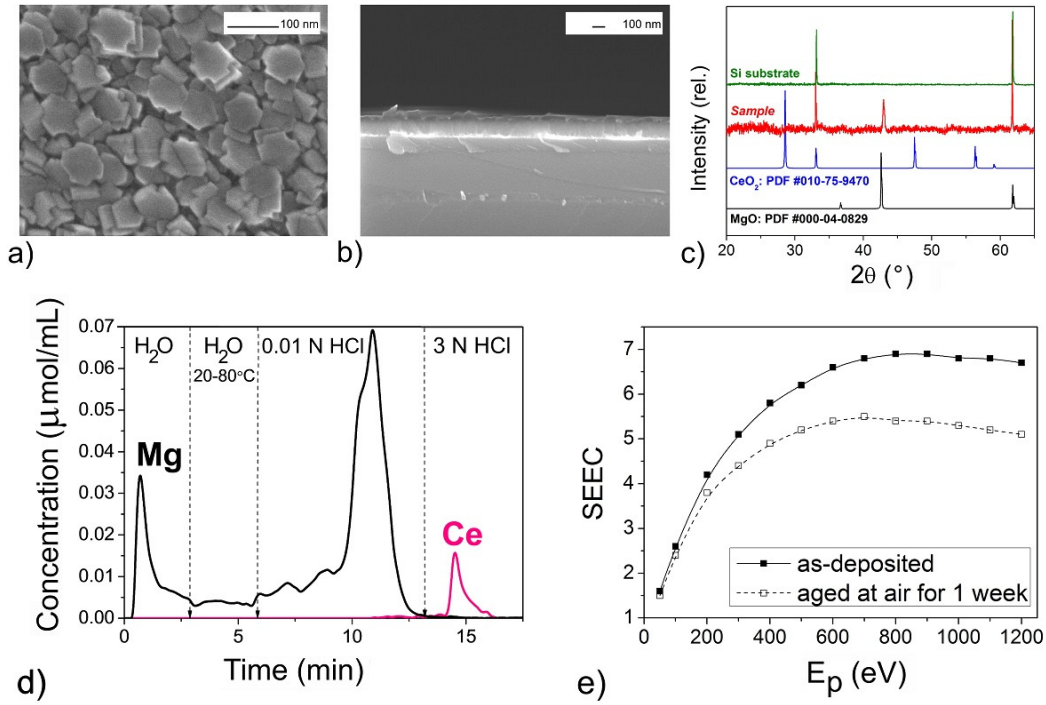


Figure 7. The mixed oxide film with n(Mg):n(Ce) = 11 according to DD data: SEM images (**a**,**b**), XRD pattern (**c**) DD curves (**d**), SEEC (Ep) curves (**e**).

Table 2. The chemical characterization of the mixed oxide films deposited by MOCVD from a combination of $Mg(tmeda)(thd)_2$ and $X(thd)_4$ precursors (X = Zr, Ce).

Figure	Metal Atomic Ratio (DD)	Carbon Content, at.% (EDX) [1]	The Main Oxide Species (DD)	Amount, Mass.%
Figure 3	Mg/Zr = 50	9	MgO_{1-x} basic surface	70
			MgO_{1-x} modified by CO_3^{2-}	10
			ZrO_{2-x} basic surface	15
			MgO_{1-x} modified by OH^-	5
Figure 4	Mg/Zr = 9	47	MgO_{1-x} basic surface	30
			MgO_{1-x} modified by CO_3^{2-}	25
			MgO–ZrO_2 nano-mixture	40
			MgO_{1-x} modified by OH^-	5
Figure 5	Mg/Zr = 11	22	MgO_{1-x} basic surface	55
			MgO_{1-x} modified by CO_3^{2-}	15
			$(ZrMg)O_x$ intermediate	25
			MgO_{1-x} modified by OH^-	5
Figure 6	Mg/Zr = 10	24	MgO_{1-x} basic surface	50
			MgO_{1-x} modified by CO_3^{2-}	25
			$(ZrMg)O_x$ intermediate	20
			MgO_{1-x} modified by OH^-	5
Figure 7	Mg/Ce = 11	24	MgO_{1-x} basic surface	50
			MgO_{1-x} modified by CO_3^{2-}	10
			CeO_{2-x} basic surface	25
			MgO_{1-x} modified by OH^-	15

[1] Carbon content in non-doped MgO film was 5 at.%.

The atomic metal ratios were determined through the complete dissolution of films with the determination of the metal content by ICP AES during the DD experiments (Table 2). The Mg/Zr and Mg/Ce ratios in the formed films strongly depend on the thermochemical characteristics of the precursors used in co-deposition, namely, on the temperature stability of the vapors. In particular, for magnesium and cerium precursors, the effective MOCVD temperature ranges coincide: >400 °C [14,63]. This indicates the efficient vapor decomposition of both compounds Mg(tmeda)$(thd)_2$ and $Ce(thd)_4$ at the deposition temperature 450 °C used here. Indeed, the Mg/Ce ratio in the obtained films is close to that specified by the mass transfer of the precursors. In contrast, the zirconium precursor has a higher thermal stability [62]. Thus, the decomposition of $Zr(thd)_4$ at 450–500 °C was not so efficient, which caused a lower zirconium content in the films. The amount of zirconium coherently increased with an increase in the deposition temperature. Notable that the sample obtained at the highest temperature and with the highest molar transfer rate of the zirconium precursor is amorphous (Figure 4). In this case, the excess CO_2 occurring from the precursor in the gas medium is adsorbed actively on the fine particles and prevents their continued growth.

One can see that DD analysis was extremely helpful in detecting the variety of the phase state and chemical composition of the oxide species in the mixed films (Figures 3d, 4d, 5d, 6d and 7d). All the DD spectra consist of several peaks indicating heterogeneous phase state of the films. The relation of these peaks with nature of oxide species modified by different defects was made based on probes shown above in Section 2. The oxide species dissolving in various solvents, from the weakest to the strongest ones, have been identified as follows and their amounts are collected in Table 2:

- dissolving in H_2O: magnesium oxide modified by hydroxyl groups (MgO_{1-x} modified by OH^-);
- dissolving in hot H_2O: magnesium oxide species modified by Fs (MgO_{1-x} basic surface);
- dissolving in 0.01 N HCl: magnesium oxide modified by Fs with upper layer modified by CO_3^{2-} (MgO_{1-x} modified by CO_3^{2-}/MgO_{1-x});
- dissolving in H_2O: nanosize, non-stoichiometric zirconium dioxides ZrO_{2-x};
- dissolving in 3 N HCl: nanosize, non-stoichiometric CeO_{2-x};
- dissolving in 4 N HF: any mixed magnesium and zirconium oxides.

In general, the profiles of the DD curves of mixed oxide films differ from those for pure MgO obtained by the same way [14]. Here, the oxide species dissolving in 0.01 N HCl were of main phase with the peaks of large area and complex form. The evolution of the peak profiles may be explained by occurrence of adsorbed CO_2 on the active Fs sites in the uppermost layer of this type of the oxide resulting in reducing content of pure active MgO_{1-x} (Figures 3d, 4d, 5d, 6d and 7d). It should be also noted that the carbon content in the samples determined by EDX, increases also with an increase of in the doping element content (Table 2). This is consistent with the idea that the precursor of the second component is the main supplier of the excess CO_2 during the film deposition. The contents of pure and poisoned oxide species were calculated from their contributions in the total areas of the complex peak using the specific program of DD [55]. These contents are presented in Table 2 where one can see that the largest amounts of the active MgO_{1-x} with the basic surface are contained in the film with the increased roughness whose morphological defects absorb the most of CO_2 molecules (Figure 3).

The DD method provides also essential information on the amount and nature of zirconium oxide present in mixed films. In particular, from the ability of Zr-oxide to dissolve in water (Figure 3d), one might expect occurrence of low-dimensional non-stoichiometric clusters of Zr-oxide distributed on the MgO surface. The joint appearance of Mg and Zr ions in solution in both HCl and HF solvents and slow dissolution kinetics indicate the formation not solid solution of (Mg,Zr)O-type, but a low-disperse mixture of magnesium and zirconium oxides mixed on the atomic level (Figure 4d). Considering that the proportion of magnesium oxide in this mixture is greater than zirconium according to quantitative

DD data, we designated this product as "MgO–ZrO_2 nano-mixture" (Table 2). For other samples, magnesium and zirconium appear together in solution only by 3N HF treatment, their dissolution curves are collinear, and this process proceeds quickly (Figures 5d and 6d). This clearly indicates the formation of some intermediate mixed products being loose layers formed at the interfaces between the nano-size oxides. Quantitative data show that the proportion of zirconium here is higher than magnesium, so we designated these phases as "$(ZrMg)O_x$ intermediates" (Table 2).

For Mg–Ce–O film, the dissolution of doped oxide in MgO is not recorded, since the profiles of the DD curves clearly show a separate dissolution of the cerium and magnesium components (Figure 7c). The non-stoichiometric oxide CeO_{2-x} detected as dissolving in 3 N HCl is most likely spatially unevenly distributed on the surface of magnesium oxide. Note that the physical mixture of the individual oxides is more typical situation for the Mg–Ce–O system [43,44]. It was impossible to determine the doping level of Zr and Ce in MgO_{1-x} because their amounts (if any) are lower than the detection limit of the analysis.

5. Discussion

The phase and chemical diversity of mixed films predetermines also the diversity of their macroscopic emission properties, which manifests not only in the maximum SEEC values and the general shapes of the SEEC- Ep curves, but also in the behavior during storage. The higher SEEC and its reducing after aging in air may be a good indicator of the presence of the active MgO with the high content (Figures 3e, 5e, 6e and 7e). It seems that the surface distribution of active ZrO_{2-x} particles contributed also in the high SEEC and its stability up to Ep = 1200 eV due to an increase in the negative charge of the surface (Figure 3e). The same effect of the presence of CeO_{2-x} on the surface of the active MgO is observed for Mg–Ce–O films (Figure 7e). One can see that the less content of active MgO the lower SEEC magnitude (Figures 5e and 6e), and it falls to 3 where the active phase is least (Figure 4e). The presence of intermediate ZrMgO intermediate products resulted in increasing stability of SEEC up to Ep = 1200 eV (Figure 5e) or decreasing (Figure 6e). The findings demonstrate that the SEE properties of the mixed films depend not only on morphological and structural features but require deep insights into their chemical state.

Based on above presented data, the preliminary results on the features the mixed oxide films of Mg–X–O systems (X = Zr, Ce) deposited by MOCVD procedure can be summarized as follows:

- During MOCVD at 450–500 °C, interaction of MgO with ZrO_2 takes place due to nanoscale and defected and disordered states both of these oxides to form mixed phases that are metastable according to the equilibrium phase diagram [51]. No interaction was between CeO_2 and MgO in similar conditions, that is in line with results of other works [43,44];
- The mixed samples with higher Zr content obtained at higher temperatures (500 °C) were highly dispersive and no peaks appear on the XRD patterns. For nanoscale crystallites, only (200) peak of the cubic MgO was observed. This XRD information was quite scant to understand what happens with oxides during deposition;
- Chemical information obtained by DD method was sufficient for assigning all the films to multiphase. These were the mixtures of individual oxide species or the Mg-oxide with intermediate $(ZrMg)O_x$ products which contribute variously in SEEC magnitude;
- The magnesium, zirconium and cerium oxide species identified by DD were related to non-stoichiometric oxides. Their defectiveness was proved through ability to dissolve in solvents with more low chemical potential than it takes for strong stoichiometric oxides;
- Amount of the oxygen defective Mg-oxide free from any sorbate defines the SEEC value, whereas the nature of the intermediate $(ZrMg)O_x$ products has an impact on the SEEC, making this value stable or unstable at high primary electron energy, E_p.
- Involving the $Zr(thd)_4$ and $Ce(thd)_4$ precursors enriched by CH_3-fragments led to appearance of the excess quantities of the undesired CO_2 gas species, which reduced

the number of the active surface sites of MgO; amount of MgO species modified by carbonate groups correlated with the amount of the second precursor involved. Therefore, to obtain mixed-oxide materials with the highest SEEC, it is necessary to select other combinations of precursors for the MOCVD process. The fairly rich chemistry of the volatile compounds of magnesium and its dopants allows us to expect a success in this task.

6. Conclusions

Following the accrescent interest in MgO-based emission film materials, this work covers two related aspects of this area. The first is a brief review of mixed film results focused on MgO doping in order to explain the improved emission characteristics. The second is the argumentation of MOCVD as a promising method for obtaining such systems, which is supported here by the primary experimental results. In addition to characterizing the obtained films by standard physical methods, we have demonstrated for the first time the capabilities of the differential dissolution chemical method for the analysis of such complex objects. In fact, this approach sheds unique light on the nature of the chemical spices that form the film and their mutual arrangement. Using this information, MOCVD procedure was found to be able to produce nanoscale and oxygen defective magnesium, zirconium and cerium oxides. Moreover, there is reason to believe that mixed ternary phases from refractory oxides MgO and ZrO_2 could form in the MOCVD process at 450–500 °C.

Thus, here we have presented the general field of activity and prospects for controlling the chemical composition of films using MOCVD. Further studies, including the precision methods of composition and structure control, will be focused on a more accurate interpretation of DD results, especially in relation to mixed phases and a determination of clear correlations of the effect of precursors and deposition conditions on the composition, microstructure, and emission properties of films. Selection of optimal precursors and process parameters will allow expanding the approaches to obtain films with stable and high SEECs.

Author Contributions: Conceptualization, I.G.V.; methodology, A.A.P., E.S.V. and I.G.V.; investigation, A.A.P. and E.S.V.; resources, A.A.P. and E.S.V.; writing—original draft preparation, I.G.V. and E.S.V.; writing—review and editing, N.B.M. and I.G.V.; visualization, E.S.V.; supervision, I.G.V.; project administration, I.G.V. All authors have read and agreed to the published version of the manuscript.

Funding: The research was funded by RFBR according to the research project NO. 18-08-01105-A.

Data Availability Statement: Not applicable.

Acknowledgments: The authors thank Sergey V. Zabuslaev for the SEEC measurements and Alexandra Yu. Struchevskaya for the participation of the precursor and film samples preparation.

Conflicts of Interest: The authors declare no conflict of interest.

References

1. Tao, S.; Chan, H.W.; Van Der Graaf, H. Secondary electron emission materials for transmission dynodes in novel photomultipliers: A review. *Materials* **2016**, *9*, 1017. [CrossRef] [PubMed]
2. Kovtunenko, P.V.; Kharif, Y.L. Non-stoichiometry of the alkaline earth metal oxides. *Russ. Chem. Rev.* **1979**, *48*, 243–261. [CrossRef]
3. Jokela, S.J.; Veryovkin, I.V.; Zinovev, A.V.; Elam, J.W.; Mane, A.U.; Peng, Q.; Insepov, Z. Secondary electron yield of emissive materials for large-area micro-channel plate detectors: Surface composition and film thickness dependencies. *Phys. Procedia* **2012**, *37*, 740–747. [CrossRef]
4. Guo, J.; Wang, D.; Xu, Y.; Zhu, X.; Wen, K.; Miao, G.; Cao, W.; Si, J.; Lu, M.; Guo, H. Secondary electron emission characteristics of Al_2O_3 coatings prepared by atomic layer deposition. *AIP Adv.* **2019**, *9*, 095303. [CrossRef]
5. Tan, H.; Xu, N.S.; Deng, S. Synthesis and electron emission properties of MgO nanowires. *J. Vac. Sci. Technol. B* **2010**, *28*, C2B20. [CrossRef]
6. Kuchumov, B.M.; Shevtsov, Y.V.; Semyannikov, P.P.; Filatov, E.S.; Igumenov, I.K. Pulsed MO CVD processes of MgO layer deposition from $Mg(thd)_2$. *ECS Trans.* **2009**, *25*, 927–934. [CrossRef]

7. Prodanović, V.; Chan, H.W.; Mane, A.U.; Elam, J.W.; Minjauw, M.M.; Detavernier, C.; Van Der Graaf, H.; Sarro, P.M. Effect of thermal annealing and chemical treatments on secondary electron emission properties of atomic layer deposited MgO. *J. Vac. Sci. Technol. A* **2018**, *36*, 06A102. [CrossRef]
8. Guo, J.; Wang, D.; Wen, K.; Xu, Y.; Zhu, X.; Liu, L.; Cao, W.; Si, J.; Lu, M.; Guo, H. Theoretical and experimental investigation of secondary electron emission characteristics of MgO coating produced by atomic layer deposition. *Ceram. Int.* **2020**, *46*, 8352–8357. [CrossRef]
9. Rajopadhye, N.; Joglekar, V.; Bhoraskar, V.; Bhoraskar, S. Ion secondary electron emission from Al_2O_3 and MgO films. *Solid State Commun.* **1986**, *60*, 675–679. [CrossRef]
10. Schleicher, F.; Taudul, B.; Halisdemir, U.; Katcko, K.; Monteblanco, E.; Lacour, D.; Boukari, S.; Montaigne, F.; Urbain, E.; Kandpal, L.M.; et al. Consolidated picture of tunnelling spintronics across oxygen vacancy states in MgO. *J. Phys. D Appl. Phys.* **2019**, *52*, 305302. [CrossRef]
11. Wang, J.; Wu, H.; Song, Z.; Li, Y.; Xu, K.; Liu, C. Influence of oxygen partial pressure on microstructure and discharge properties of Mg–Zr–O protective films deposited by magnetron sputtering. *J. Vac. Sci. Technol. A* **2010**, *28*, 88–93. [CrossRef]
12. Choy, K.-L. Chemical vapour deposition of coatings. *Prog. Mater. Sci.* **2003**, *48*, 57–170. [CrossRef]
13. O'Mahony, A.; Craven, C.A.; Minot, M.J.; Popecki, M.A.; Renaud, J.M.; Bennis, D.C.; Bond, J.L.; Stochaj, M.E.; Foley, M.R.; Adams, B.W.; et al. Atomic layer deposition of alternative glass microchannel plates. *J. Vac. Sci. Technol. A* **2016**, *34*, 01A128. [CrossRef]
14. Vasilyeva, I.G.; Vikulova, E.S.; Morozova, N.B.; Pochtar, A.A.; Igumenov, I.K. Invisible surface oxygen vacancies in a thin MgO Film: Impacts on the chemical activity and secondary electron emission. *Inorg. Chem.* **2020**, *59*, 17999–18009. [CrossRef]
15. Vikulova, E.S.; Pochtar, A.A.; Morozova, N.B.; Vasilyeva, I.G. Features of the MOCVD formation of MgO−RuO_2 electron-emitting film structures. *J. Struct. Chem.* **2019**, *60*, 1352–1360. [CrossRef]
16. Lukashov, V.; Abdrakhmanov, R.; Vasilieva, I.; Igumenov, I. Gradient ceramic structures formation from an impact jet of vapors of organometallic compounds flowing onto the hot barrier. *J. Physics Conf. Ser.* **2019**, *1382*, 012061. [CrossRef]
17. Wei, Q.; Wu, S.; Li, J.; Hu, W.; Zhang, J. Preparation of MgO/Au multilayer composite films and related studies on secondary electron emission effect. *J. Electron. Mater.* **2018**, *47*, 385–393. [CrossRef]
18. Li, J.; Hu, W.; Hao, L.; Gao, B.; Wu, S.; Zhang, J.; Li, Y. Secondary electron emission enhancement of MgO/Au composite film by adopting a gold buffer layer. *Mater. Res. Bull.* **2019**, *118*, 110493. [CrossRef]
19. Zhou, F.; Zhang, Q.; Wang, F.; Wang, J.; Yang, Y.; Lai, C.; Liu, W.; Wang, J. Surface characterization and secondary electron emission properties of alumina containing MgO film on Ag-Mg-Al alloy. *Metals* **2018**, *8*, 570. [CrossRef]
20. Gao, B.; Li, J.; Hu, W.; Hao, L.; Wu, S.; Li, Y.; Fan, H. Analysis of secondary electron emission properties of MgO/Au composite film with an Al-doped MgO surface layer. *AIP Adv.* **2018**, *8*, 115031. [CrossRef]
21. Wang, F.; Zhou, F.; Wang, J.; Liu, W.; Zhang, Q.; Yin, Q. Characterization of MgO/Al_2O_3 composite film prepared by DC magnetron sputtering and its secondary electron emission properties. *J. Electron. Mater.* **2018**, *47*, 4116–4123. [CrossRef]
22. Li, J.; Hu, W.; Hao, L.; Wu, S.; Zhang, J. Influence of the substrate temperature on the microstructure and electron-induced secondary electron emission properties of MgO/Au composite film. *Mater. Res. Bull.* **2018**, *100*, 308–312. [CrossRef]
23. Li, J.; Hu, W.; Hao, L.; Gao, B.; Wu, S.; Zhang, J.; Li, Y.; Fan, H. Electron-induced secondary electron emission of Zn-doped MgO/Au composite film. *Mater. Lett.* **2018**, *229*, 360–363. [CrossRef]
24. Li, J.; Hu, W.; Wang, K.; Gao, B.; Li, Y.; Wu, S.; Zhang, J.; Fan, H. Au doping effect on the secondary electron emission performance of MgO films. *Materials* **2018**, *11*, 2104. [CrossRef] [PubMed]
25. Li, M.; Xu, M.; Zou, J.; Tao, H.; Wang, L.; Zhou, Z.; Peng, J. Realization of Al_2O_3/MgO laminated structure at low temperature for thin film encapsulation in organic light-emitting diodes. *Nanotechnology* **2016**, *27*, 494003. [CrossRef]
26. Yu, H.K.; Kim, W.-K.; Park, E.C.; Kim, J.S.; Koo, B.-W.; Kim, Y.-W.; Ryu, J.H.; Lee, J.-L. Enhanced secondary electron emission in nanoscale thin metal containing MgO film: Laser irradiation on creation of F centers. *J. Phys. Chem. C* **2011**, *115*, 17910–17914. [CrossRef]
27. Lee, J.W. Calculation of the secondary electron emission coefficients of MgO, MgBeO, MgCaO, MgSrO and MgBaO induced by auger neutralization of He^+, Ne^+, Ar^+ and Xe^+ ions. *New Phys. Sae Mulli* **2018**, *68*, 939–944. [CrossRef]
28. Lee, J.; Ko, J.-H. Defect states of transition metal-doped MgO for secondary electron emission of plasma display panel. *J. Inf. Disp.* **2014**, *15*, 157–161. [CrossRef]
29. Rodriguez, J.A. Orbital-band interactions and the reactivity of molecules on oxide surfaces: From explanations to predictions. *Theor. Chem. Acc.* **2002**, *107*, 117–129. [CrossRef]
30. Kim, D.H.; Kim, S.H.; Choi, I.S.; Lee, J. 36.3: Secondary electron emission coefficient of pure and Cs-doped MgO for low energy noble gas ions. *SID Symp. Dig. Tech. Pap.* **2014**, *37*, 1392–1394. [CrossRef]
31. Yu, H.K.; Kim, J.S.; Ryu, J.H.; Kim, W.-K.; Lee, J.-L. P-90: The effect of doping to MgO protection layer on secondary electron emission property. *SID Symp. Dig. Tech. Pap.* **2014**, *37*, 544–546. [CrossRef]
32. Ahn, S.I.; Uchiike, H.; Ahn, M.H.; Kwon, S.J. The analysis of memory margin of an alternative current-plasma display panel with K-ion-doped MgO. *Mol. Cryst. Liq. Cryst.* **2009**, *499*, 290–612. [CrossRef]
33. Ahn, S.I.; Lee, S.E.; Ryu, S.H.; Choi, K.C.; Kwon, S.J.; Uchiike, H. A study on the secondary electron emission from Na-ion-doped MgO films in relation to the discharge characteristics of plasma display panels. *Thin Solid Films* **2009**, *517*, 1706–1709. [CrossRef]
34. Cho, J.; Park, J.-W. Effect of CaO addition on properties of ion-induced secondary electron emission of MgO films. *J. Vac. Sci. Technol. A* **2000**, *18*, 329–333. [CrossRef]

35. Yu, H.K. Secondary electron emission properties of Zn-doped MgO thin films grown via electron-beam evaporation. *Thin Solid Films* **2018**, *653*, 57–61. [CrossRef]
36. Kim, R.; Kim, Y.; Park, J.-W. Influence of densification of the protective layer on the discharge voltage in AC plasma display panel. *Vacuum* **2001**, *61*, 37–43. [CrossRef]
37. Kim, R.; Kim, Y.; Park, J.-W. Improvement of secondary electron emission property of MgO protective layer for an alternating current plasma display panel by addition of TiO_2. *Thin Solid Films* **2000**, *376*, 183–187. [CrossRef]
38. Rodriguez, J.A.; Jirsak, T.; Perez, M.; Chaturvedi, S.; Kuhn, M.; González, L.; Maiti, A. Studies on the behavior of mixed-metal oxides and desulfurization: Reaction of H_2S and SO_2 with Cr_2O_3(0001), MgO(100), and $Cr_xMg_{1-x}O$(100). *J. Am. Chem. Soc.* **2000**, *122*, 12362–12370. [CrossRef]
39. Jung, E.Y.; Park, C.-S.; Hong, T.E.; Sohn, S.H. Effects of Sc- and Zr-doped MgO layers on electron emission and discharge characteristics of alternating-current plasma display panels. *Jpn. J. Appl. Phys.* **2014**, *53*, 36002. [CrossRef]
40. Ivanova, A.; Moroz, B.; Moroz, E.; Larichev, Y.; Paukshtis, E.; Bukhtiyarov, V.I. New binary systems Mg–M–O (M=Y, La, Ce): Synthesis and physico-chemical characterization. *J. Solid State Chem.* **2005**, *178*, 3265–3274. [CrossRef]
41. Gvozd', V.S. Structure and properties of periclase ceramics doped with rare-earth oxides. *Glas. Ceram.* **1993**, *50*, 482–485. [CrossRef]
42. Kumar, A.; Thota, S.; Sivakumar, S.; Priya, S.; Kumar, J. Sol–gel synthesis and optical behavior of Mg–Ce–O nano-crystallites. *J. Sol-Gel Sci. Technol.* **2013**, *68*, 46–53. [CrossRef]
43. Torres-Huerta, A.M.; Brachetti-Sibaja, S.B.; Dominguez-Crespo, M.A.; Ramirez-Meneses, E.; Arenas-Alatorre, J.A. Electrochemical evaluation of MgO-CeO_2 coatings on AA6066 aluminum alloy by MOCVD. *ECS Trans.* **2009**, *20*, 447–458. [CrossRef]
44. Bernal, S.; Baker, R.T.; Burrows, A.; Calvino, J.J.; Kiely, C.J.; López-Cartes, C.; Pérez-Omil, J.A.; Rodríguez-Izquierdo, J.M. Structure of highly dispersed metals and oxides: Exploring the capabilities of high-resolution electron microscopy. *Surf. Interface Anal.* **2000**, *29*, 411–421. [CrossRef]
45. Kumar, A.; Thota, S.; Deva, D.; Kumar, J. Ion-induced secondary electron emission, optical and hydration resistant behavior of MgO, Mg–Mo–O and Mg–Ce–O thin films. *Thin Solid Films* **2014**, *556*, 260–269. [CrossRef]
46. Maiti, P.; Das, P.S.; Bhattacharya, M.; Mukhopadhyay, A.K.; Saha, B.; Mullick, A.K.; Mukhopadhyay, A.K. Transparent Al^{+3} doped MgO thin films for functional applications. *Mater. Res. Express* **2017**, *4*, 086405. [CrossRef]
47. Buyakova, S.P.; Kalatur, E.S.; Buyakov, A.S.; Kulkov, S.S. Structure and properties of ZrO_2–MgO powders. *IOP Conf. Ser. Mater. Sci. Eng.* **2016**, *123*, 012040. [CrossRef]
48. Song, Z.; Wang, J.; Li, Y.; Xu, K.; Liu, C. Effect of aging on microstructure and discharging property of Mg-Zr-O protective films for alternating current plasma display panel. *Phys. Procedia* **2012**, *32*, 814–821. [CrossRef]
49. Guo, B.; Liu, C.; Song, Z.; Liu, L.; Fan, Y.; Xia, X.; Fan, D. Influence of ZrO_2 addition on the microstructure and discharge properties of Mg–Zr–O protective layers in alternating current plasma display panels. *J. Appl. Phys.* **2005**, *98*, 043304. [CrossRef]
50. Kim, S.S. Thermodynamic modeling of the Sc_2O_3–MgO phase diagram. *J. Alloy. Compd.* **2009**, *488*, 479–481. [CrossRef]
51. Śnieżek, E.; Szczerba, J.; Stoch, P.; Prorok, R.; Jastrzebska, I.; Bodnar, W.; Burkel, E. Structural properties of MgO–ZrO_2 ceramics obtained by conventional sintering, arc melting and field assisted sintering technique. *Mater. Des.* **2016**, *99*, 412–420. [CrossRef]
52. Kumar, A.; Kumar, J. On the synthesis and optical absorption studies of nano-size magnesium oxide powder. *J. Phys. Chem. Solids* **2008**, *69*, 2764–2772. [CrossRef]
53. Pathak, N.; Gupta, S.K.; Prajapat, C.L.; Sharma, S.K.; Ghosh, P.S.; Kanrar, B.; Pujari, P.; Kadam, R.M. Defect induced ferromagnetism in MgO and its exceptional enhancement upon thermal annealing: A case of transformation of various defect states. *Phys. Chem. Chem. Phys.* **2017**, *19*, 11975–11989. [CrossRef] [PubMed]
54. Heo, S.; Cho, E.; Lee, H.-I.; Park, G.S.; Kang, H.J.; Nagatomi, T.; Choi, P.; Choi, B. Band gap and defect states of MgO thin films investigated using reflection electron energy loss spectroscopy. *AIP Adv.* **2015**, *5*, 077167. [CrossRef]
55. Malakhov, V.V.; Vasilyeva, I.G. Stoichiography and chemical methods of phase analysis of multielement multiphase compounds and materials. *Russ. Chem. Rev.* **2008**, *77*, 370–392. [CrossRef]
56. Vasilyeva, I.G.; Asanov, I.P.; Kulikov, L.M. Experiments and consideration about surface nonstoichiometry of few-layer MoS_2 prepared by chemical vapor deposition. *J. Phys. Chem. C* **2015**, *119*, 23259–23267. [CrossRef]
57. Vikulova, E.S.; Zherikova, K.V.; Korolkov, I.V.; Zelenina, L.N.; Chusova, T.P.; Sysoev, S.V.; Alferova, N.I.; Morozova, N.B.; Igumenov, I.K. Thermal properties of mixed-ligand magnesium complexes with beta-diketonates and diamimes as potential MOCVD precursors. *J. Therm. Anal. Calorim.* **2014**, *118*, 849–856. [CrossRef]
58. Zelenina, L.N.; Chusova, T.P.; Zherikova, K.V.; Nazarova, A.A.; Igumenov, I.K. Thermal study of CVD metal–organic precursors. *J. Therm. Anal. Calorim.* **2018**, *133*, 1157–1165. [CrossRef]
59. Schlupp, M.V.F.; Martynczuk, J.; Prestat, M.; Gauckler, L.J. Precursor Decomposition, microstructure, and porosity of yttria stabilized zirconia thin films prepared by aerosol-assisted chemical vapor deposition. *Adv. Energy Mater.* **2013**, *3*, 375–385. [CrossRef]
60. Hatanpää, T.; Ihanus, J.; Kansikas, J.; Mutikainen, I.; Ritala, M.; Leskela, M. Properties of $[Mg_2(thd)_4]$ as a precursor for atomic layer deposition of MgO thin films and crystal structures of $[Mg_2(thd)_4]$ and $[Mg(thd)_2(EtOH)_2]$. *Chem. Mater.* **1999**, *11*, 1846–1852. [CrossRef]
61. Qin, X.; Zaera, F. Chemistry of ruthenium diketonate atomic layer deposition (ALD) precursors on metal surfaces. *J. Phys. Chem. C* **2018**, *122*, 13481–13491. [CrossRef]

62. Turgambaeva, A.E.; Zherikova, K.V.; Mosyagina, S.A.; Igumenov, I.K. A study of the thermal behavior of the system of zirconium and neodymium dipyvaloylmethanates. *Russ. J. Appl. Chem.* **2017**, *90*, 1062–1067. [CrossRef]
63. Sawka, A.; Kwatera, A.; Andreasik, P. Deposition and characterization of ceria layers using the MOCVD method. *Mater. Lett.* **2017**, *204*, 39–41. [CrossRef]